# Structure and photoluminescent features of di-amide cross-linked alkylene/siloxane hybrids

S. C. Nunes[a], V. de Zea Bermudez[a]*, J. Cybinska[b], R. A. Sá Ferreira[b], L. D. Carlos[b], M. M. Silva[c], M. J. Smith[c], D. Ostrovskii[d], J. Rocha[e]

***Receipt/Acceptance Data*** **[DO NOT ALTER/DELETE THIS TEXT]**
***Publication data*** **[DO NOT ALTER/DELETE THIS TEXT]**
**DOI: 10.1039/b000000x [DO NOT ALTER/DELETE THIS TEXT]**

Novel amide cross-linked alkylene/siloxane hybrid materials (di-amidosils) synthesized by the sol-gel process have been investigated. Two samples identified by the notation d-A(x) with x = 4 and 8 (where x is the number of methylene groups of the alkylene chain) have been produced as transparent, amorphous, rigid monoliths, thermally stable up to about 381 and 400 ºC, respectively. In the d-A(8) hybrid the siliceous framework is composed of $[(SiO)_3Si(CH_2)\text{-}]$ and $[(SiO)_2(HO)Si(CH_2)\text{-}]$ substructures. Structural unit distances of 4.1 and 4.2 Å and average interparticle distances of 12 and 17 Å have been determined for d-A(4) and d-A(8), respectively. In these compounds the alkyl chains are disordered and adopt *gauche* conformations. While a negligible proportion of the amide linkages remain non-bonded, the great majority of these groups belong to highly disordered strong hydrogen-bonded amide-amide associations. The hybrids introduced are room temperature white light emitters, presenting an emission large, broad band in the blue/purplish-blue spectral region. The origin of such band have been ascribed to the convolution of donor-acceptor pair (D-A) recombinations that occur in the NH groups of the urea linkages and in the siliceous nanodomains. The maximum quantum yield value of the d-A(8) di-amidosil is 5.4 %.

## Introduction

Organic/inorganic hybrids[1] are an emerging class of innovative nanostructured materials with tailored properties - seldom seen in other types of materials - and unparalleled performances suitable for a wide range of practical applications.[2-4] The main route for the formation of such advanced systems is the sol-gel method.[5] This versatile synthetic process, which involves the hydrolysis and condensation of precursor molecules (typically alkoxides) under mild conditions, allows the chemical design of pure and well-controlled multifunctional hybrid materials in which organic, inorganic, and even biological components are mixed at the nanosize level. The products can be produced in a variety of physical forms, including coatings, monoliths, composites, fibres and nanoparticles depending on several parameters (e.g., water and alcohol contents, type of catalyst, solution pH, rate of drying, nature of precursors). In the class of hybrid materials two subclasses can be distinguished on the basis of the connection that is established between the organic and inorganic components: if the organic molecules are embedded within the inorganic matrix through weak interactions (e.g. hydrogen bonding, van der Waals contacts, π-π interactions or electrostactic forces) the materials are included Class I hybrids; if the both components are linked by means of strong bonds (e.g. covalent, ionic-covalent or Lewis acid-base bonds) the materials belong to Class II.

In the last few years the hybrid strategy has been increasingly adopted for the development of low cost matrices, especially of the siloxane-based type, with attractive optical features for optical switching and data storage devices,[6] photoelectrochemical cells and coatings for solar energy conversion,[7] hybrid materials having high laser efficiencies and good photostability,[8] photopattern waveguiding structures for integrated optics[9,10] and electroluminescent diodes.[11,12] Several stable and efficient white-light photoluminescent amine-functionalized hybrids lacking metal activator ions have been introduced.[13-19] One of the highest external photoluminescence (PL) quantum yields reported up to date is that of the amine propyltriethoxysilane (APTES)-formic acid hybrid (35±1 %).[13] The APTES-acetic acid phosphor analog exhibits two distinct emissions with quantum yields of 21 and 12 %.[14] The latter values are of the same order of magnitude as those estimated for Class II di-urea and di-urethane cross-linked poly(oxyethylene) (POE)/siloxane hybrid frameworks.[17,18]

We demonstrated recently that the white-light PL of the latter structures, designated as di-ureasils and di-urethanesils, respectively, results from a convolution of the emission originated in the NH groups of the urea (-NHC(=O)NH-) and urethane (-NHC(=O)O-) groups, respectively, with electron-hole recombinations occurring within the siloxane nanoclusters.[19] These components reveal a radiative recombination mechanism typical of donor-acceptor pairs, mediated by some localized centers. The NH-related component was associated with photo-induced proton-transfer between $NH_2^+$ and $N^-$ defects.[19] The siliceous nanodomains-related component was ascribed to oxygen-related defects.[19] In an attempt to gain more insight into the mechanisms responsible for the photonic properties of both hybrid matrices, we decided to examine in the present work a

† Electronic Supplementary Information (ESI) available: [details of any supplementary information available should be included here]. See http://www.rsc.org/suppdata/xx/b0/b000000x/

* vbermude@utad.pt

family of structurally simpler hybrid analog materials named *di-amidosils*.

The di-amidosils are novel Class II di-amide cross-linked alkylene/siloxane xerogels in which alkylene chains with variable length are bonded at both ends to a siliceous framework through amide (-NHC(=O)-) groups. X-ray Diffraction (XRD), $^{13}C$ cross-polarization (CP)/Magic Angle Spinning (MAS) and $^{29}Si$ MAS Nuclear Magnetic Resonance (NMR), Differential Scanning Calorimetry (DSC), Thermogravimetric Analysis (ATG), Fourier-Transform infrared (FTIR), FT-Raman, and photoluminescence (PL) spectroscopies to investigate the structure, morphology, thermal properties, packing and conformations of the alkylene chains, hydrogen bonding and optical features.

## Experimental

### Materials

Ethanol ($CH_3CH_2OH$, Merck), pyridine (py, Aldrich) and tetrahydrofuran (THF, Merck) were stored over molecular sieves. Amberlyst A-21 Ion-Exchange Resin (Aldrich) was washed with THF and stored in an oven at 80 ºC. Adipoyl chloride ($ClC(=O)-(CH_2)_4C(=O)Cl$, AC, Aldrich), sebacoyl chloride ($ClC(=O)-(CH_2)_8C(=O)Cl$, SC, Aldrich), and 3-aminopropyl)triethoxysilane ($(CH_3CH_2O)_3Si(CH_2)_3NH_2$, APTES, Fluka) were used as received. High purity distilled water ($H_2O$) was used in all experiments.

### Synthesis

The preliminary stage of the preparation of the di-amidosils involved the formation of an amide cross-link between the Cl group of AC and SC and the $NH_2$ group of APTES to yield organic-inorganic hybrid precursors designated as d-amidepropyltriethoxisilanes (d-ADPTES(x), with x = 4 and 8, respectively) (Scheme 1). In the second stage of the synthetic procedure, a mixture of $CH_3CH_2OH$ and $H_2O$ was added to d-ADPTES(x) to promote the hydrolysis and condensation reactions characteristic of the sol-gel process (Scheme 1).

*Step 1:* A volume of 0.5 ml of AC (3.44 mmol) (1 ml of SC (4.69 mmol)) was added to a solution prepared through the addition of 1.604 ml (6.88 mmol) (2.187 ml (9.38 mmol)) of APTES to a 40-ml THF solution containing 111 µl (1.37 mmol) (152 µl (1.876 mmol)) of py and 1.756 g (8.25 mmol) (2.4 g (11.24 mmol)) of Amberlyst resin (molar ratio APTES: $ClC(=O)(CH_2)_xC(=O)Cl$: Amberlyst resin: py = 2:1:1.2:0.2). The resulting mixture was sealed and stirred under nitrogen ($N_2$) atmosphere for 10 hours at room temperature. The grafting process was infrared monitored. The intensity of the band attributed to the stretching vibration of the C=O group of the chloride acid, located at 1796 $cm^{-1}$ in the spectrum of AC (1801 $cm^{-1}$ in that of SC), was progressively reduced, until it disappeared upon completion of the reaction. In parallel, a series of new bands, associated with the vibrations characteristic of the amide group, appeared in the 1760-1530 $cm^{-1}$ spectral interval. The solution was filtrated and the solvent evaporated. The d-ADPTES(4) and d-ADPTES(8) precursors, produced as oils, were dried under vacuum for several hours. Their structure, depicted in Scheme 1, was confirmed by means of $^1H$ NMR ($CDCl_3$, 400.13 MHz) (Table I) [20-24], $^{13}C$ NMR ($CDCl_3$, 100.62 MHz) (Table I)[20-25] and FTIR ($cm^{-1}$): d-ADPTES(4): 3312 (νNH), 3088 (νNH), 2919 ($\nu_aCH_2$), 2851 ($\nu_sCH_2$), 1732 (νC=O), 1640 (νC=O), 1551 (δNH); d-ADPTES(8): 3275 (νNH), 3075 (νNH) 2929 ($\nu_aCH_2$), 2825 ($\nu_sCH_2$), 1735 (νC=O), 1642 (νC=O), 1552 (δNH).

*Step 2*: The d-ADPTES(4) and d-ADPTES(8) precursors were dissolved in 10 ml of THF. A volume of 1.604 ml (27.51 mmol) (2.188 ml (37.52 mmol)) of $CH_3CH_2OH$ and 248 µl (13.75 mmol) (338µl (18.76 mmol)) of $H_2O$ were added to this solution (molar ratio APTES: $CH_3CH_2OH$: $H_2O$ = 1:4:2). The resulting mixture was stirred in a sealed flask for 30 min and then cast to a Teflon mould, which was covered with Parafilm and left in a fume cupboard for 24 h. The mould was then transferred to an oven at 50 ºC and the sample was aged for a period of two weeks. The di-amidosils were produced as transparent, rigid monoliths with a yellowish hue. The d-A(x) di-amidosils were identified using the notation d-A(x), where d represents di and A represents the group amide.

### Experimental Techniques

The XRD patterns were recorded at room temperature with a Rigaku Geigerflex D/max-c diffractometer system using monochromated $CuK_\alpha$ radiation (λ = 1.54 Å) over the 2θ range of between 4 and 80 º at a resolution of 0.05 º. The d-A(4) and d-A(8) samples, analyzed as a film and a powder, respectively, were not submitted to any thermal pre-treatment.

The $^1H$ and $^{13}C$ NMR spectra were recorded in $CDCl_3$ on a Brüker ARX400 NMR spectrometer (400.13 MHz and 100.62 MHz, respectively) at CACTI-Universidad de Vigo (Spain). Chemical shifts, δ, are quoted in ppm from tetramethylsilane (TMS). $^{29}Si$ magic-angle spinning (MAS) and $^{13}C$ cross-polarization (CP) MAS NMR spectra were recorded on a Brüker Avance 400 (9.4 T) spectrometer at 79.49 and 100.62 MHz, respectively. $^{29}Si$ MAS NMR spectra were recorded with 2 µs (θ ≈30 º) rf pulses, and recycle delay of 60 s and at a 5.0 kHz spinning rate. $^{13}C$ CP/MAS NMR spectra were recorded with 4 µs $^1H$ 90º pulse, 2 ms contact time, a recycle delay of 4 s and at a spinning rate of 8 kHz. Chemical shifts (δ) are quoted in ppm from TMS. Due to the extreme rigidity of the d-A(4) sample, it was not possible to transform it into a powder and thus it was not analyzed by NMR.

DSC measurements were obtained in a DSC131 Setaram DSC. A disk sections with masses of approximately 20 mg was removed from the ormolyte, placed in 40 µl aluminium cans and stored in a dessicator over phosphorous pentoxide ($P_2O_5$) for one week at room temprature under vacuum. After the drying treatment the cans were hermetically sealed and the thermograms were recorded. Each sample was heated from -100 to 250 ºC at 10 ºC $min^{-1}$. The purge gas used in all experiments was purity nitrogen ($N_2$) supplied at a constant 35 $cm^3$ $min^{-1}$ flow rate.

Samples for thermogravimetric studies were transferred to open platinum crucibles and analysed using a Rheometric Scientific TG 1000 thermobalance at a heating rate of 10º $min^{-1}$ using high purity $N_2$ as purging gas (20 ml/min). Prior to measurement, the xerogels were vacuum-dried at 80 ºC for about 48 h and kept in an argon-filled glove box.

FTIR spectra were acquired at room temperature using a Bruker 22 (Vektor) spectrometer placed inside a glove-box with a

dry argon atmosphere. The spectra were collected over the 4000-400 $cm^{-1}$ range by averaging 150 scans at a spectral resolution of 2 $cm^{-1}$. Solid samples (2 mg) were finely ground, mixed with approximately 175 mg of dried potassium bromide (Merck, spectroscopic grade) and pressed into pellets. Prior to recording the spectra, the pellets were first vacuum dried at 80-90 ºC for about 60 h, in order to reduce the levels of adsorbed water and solvent, and then transferred into a glove-box.

The FT-Raman spectra were recorded at room temperature with a Bruker IFS-66 spectrometer equipped with a FRA-106 Raman module and a near-infrared YAG laser with wavelength 1064 nm. The spectra were collected over the 3200-300 $cm^{-1}$ range at a resolution of 2 $cm^{-1}$. The accumulation time for each spectrum was 4 hours.

To evaluate complex band FTIR and FT-Raman envelopes and to identify underlying spectral components, the iterative least-squares curve-fitting procedure in the PeakFit† software was used extensively throughout this study. The best fit of the experimental data was obtained by varying the frequency, bandwidth and intensity of the bands. Taking into account the morphology of materials under investigation we decided to employ Gaussian band shapes. Owing to the disordering, which causes statistical distribution of the oscillators, the experimentally observed band shapes are very often changed from the natural Lorentzian shape to the Gaussian form. As a consequence, typical band profiles observed in solid disordered materials tend to adopt a Gaussian shape. Although it is in general accepted that in such cases the peaks are best fitted with a Voigt shape (a mixture of Lorentzian and Gaussian contributions), the use of this function is not straightforward and may lead to ambiguous results due to the possibility of different Gaussian-Lorentzian proportions.

The photoluminescence in steady-state and time resolved modes were recorded between 14 and 300 K on a modular double grating excitation spectrofluorimeter with a TRIAX 320 emission monochromator (Fluorolog-3, Jobin Yvon-Spex) coupled to a R928 Hamamatsu photomultiplier, using the front face acquisition mode. All the steady-state spectra were corrected for optics and detection spectral response.

The absolute emission quantum yields ($\phi$) were measured at room temperature using the powdered sample technique described by Brill *et al.*[26] through the following expression:

$$\phi = \left(\frac{1-r_{st}}{1-r_x}\right)\left(\frac{A_x}{A_{st}}\right)\phi_{st} \qquad (1)$$

where $r_{st}$ and $r_x$ are the diffuse reflectance (with respect to a fixed wavelength) of the hybrids and of the standard phosphor, respectively, and $\phi_{st}$ is the quantum yield of the standard phosphor. The terms $A_x$ and $A_{st}$ represent the area under the di-amidosils and the standard phosphor emission spectra, respectively. Emission and diffuse reflectance spectra were acquired with the experimental setup used to detect the photoluminescence data. Powder size and packing fraction are crucial factors because $r_{st}$, $r_x$ $A_x$ and $A_{st}$ depend on them. The di-amidosils and the phosphor standard were thoroughly ground until $r_x$ totally overlaps $r_{St}$ at a wavelength not absorbed by the nanohybrids (720 nm), thus indicating a similar powder size and packing fraction. Diffuse reflectance and emission spectra were acquired with the experimental setup aforementioned to detect the photoluminescence data. In order to have absolute intensity values $BaSO_4$ was used as reflecting standard ($r$ = 91%). The same experimental conditions, namely, position of the hybrids/standard holder, excitation and detection monochromator' slits 0.5 mm and optical alignment, were fixed. To prevent insufficient absorption of the exciting radiation, a powder layer around 3 mm was used and great care was taken in order to ensure that only the sample was illuminated, in order to diminish the quantity of light scattered by the front sample holder. The standard phosphor used was sodium salicylate (Merck P.A.), the emission spectra of which contains a large broad band peaking around 425 nm, with a constant ϕ value (60 %) for excitation wavelengths between 220 and 380 nm. These properties render sodium salicylate an adequate standard for ultra-violet (UV) absorbing samples, such as the di-amidosil. Three measurements were carried out, so that the presented $\phi$ value corresponds to the arithmetic mean value. The errors in the quantum yield values associated with this technique were estimated to be within 10 %.

## Results and Discussion

**Structure, morphology and thermal properties of di-amidosils** - The $^{13}C$ CP/MAS and $^{29}Si$ MAS NMR spectra of the d-A(8) are reproduced in Figs. 1(a) and (b), respectively. The position (δ) and assignment [20-25] of the resonance peaks are given in Table II

The $^{13}C$ CP/MAS spectrum of the d-A(8) di-amidosil is dominated by a peak centered around 29 ppm, due to the resonance of the $C^9$ carbon atoms of the alkylene chains (Fig. 1(a), Scheme 1 and Table II), revealing that the alkylene chains adopt gauche conformations.[27] The shoulder detected at about 25 ppm is ascribed to the $C^7$ methylene carbon atoms of the polymer chains (Scheme 1 and Table II). Another peak associated with the $CH_2$-based chains is found at 35 ppm ($C^6$) (Scheme 1 and Table II). The signal characteristic of the amide carbonyl group ($C^8$) appears at 174 ppm. The resonances due to the Si-bonded propyl chains are observed at 42 ($C^3$), 26 ($C^2$) and 11 ppm ($C^1$). These findings provide evidence no cleavage of the functional groups of the d-ADPTES(8) precursor molecule (alkylene and propyl chains and amide cross-links) occurred during the second stage of the synthetic procedure. The absence of the peaks associated with the resonance of the ethoxy atoms around 58 ppm ($C^4$) and 18 ppm ($C^5$) (Table I and Scheme 1) demonstrates that the hydrolysis reaction was complete.

The most prominent features of the $^{29}Si$ CP/MAS NMR spectrum of the d-A(8) hybrid are two broad signals centered at -58.8 and -67.8 ppm (Fig. 1(b) and Table II), ascribed to $T^2$ ((R-$Si(OSi)_2(OR)$) and $T^3$ ((R-$Si(OSi)_3$)) sites, respectively. $T^n$ is the conventional silicon notation (n = 1, 2 and 3, where n is the number of Si-bridging oxygen atoms). The $T^1$ ((R-$Si(OSi)(OR)_2$)) environment (-51.6 ppm) is almost negligible. The polycondensation rate c (c = 1/3 (%$T^1$ + 2%$T^2$ + 3%$T^3$)) calculated for the d-A(8) hybrid (82 %) is considerably lower than that of the di-ureasil analog (96%)[28], but practically identical to that of the corresponding di-urethanesil matrix (85%)[29]. The empirical formula (($R_{0.5}Si(OH)_{0.5}(O)_{1.2}$) of the d-A(8) sample, derived from the $^{13}C$ CP/MAS and $^{29}Si$ MAS NMR data (Table II), leads us to suggest that the structure of this di-amidosil is that tentatively represented in Scheme 2.

The XRD patterns of the di-amidosils with x = 4 and 8 are represented in Fig. 2. These diffractograms exhibit a broad band, Gaussian in shape, centered around 21.7 and 21.1 º respectively, associated with ordering within the siloxane domains.[30] The second-order of these peaks appears as a broad weak hump centered around 42 º (Fig. 2). Structural unit distances of 4.1 and 4.2 Å were calculated for these hybrids, respectively, using the Bragg law. In the XRD patterns of d-A(4) and d-A(8) a low-intensity peak is also identified at ca. 7 and 5 º , respectively (Fig. 2). Such peaks can be ascribed to interparticle scattering interference.[18,30] From the peak maximum position an average interparticle distance of 12 and 17 Å may be estimated, respectively. The lower interdomain distance observed for d-A(4) with respect to d-A(8) may be correlated with the fact that the former hybrid incorporates shorter polymer chain than the latter di-amidosil. It was previously demonstrated for similar organic-inorganic hybrids, such as the di-ureasils, that the position of this low-angle peak depends on the polymer chain length, decreasing monotonically as the chains become progressively longer.[31] The coherent length L over which the structural unit survives in the di-amidosils was estimated using the modified Scherrer equation:

$$L = I \lambda / (A \cos\theta) \quad (2)$$

where A, in radians, is the integrated area of the peaks and I its intensity. Coherent lengths of 8 and 9 Å were derived for d-A(4) and d-A(8), respectively. These values of L are approximately the same as that reported for the di-ureasils.[18]

The DSC curves of the di-amidosils depicted in Fig. 3(a) corroborate the conclusion drawn from XRD data that the materials are entirely amorphous. In the TGA curve of the d-A(4) hybrid a slight mass loss is detected at 79.2 ºC, followed by a abrupt mass loss at 381 ºC (Fig. 3(b)). The d-A(8) material also undergoes two degradation processes: decomposition starts with a slight mass loss at about 245 ºC that proceeds with an abrupt change at approximately at 400ºC.

**Chain packing and conformation** – To gather structural and phase-state information on the alkylene chains of the di-amidosils we inspected the following diagnostic modes of the hydrocarbon chains: (1) the symmetric and asymmetric $CH_2$ modes ($\nu_sCH_2$ and $\nu_aCH_2$, respectively); (2) the $CH_2$ bending ($\delta CH_2$) vibration. The FT-Raman spectra of the d-A(4) and d-A(8) nanocomposites in the $\nu_sCH_2$ and $\nu_aCH_2$ regions are reproduced in Fig 4. The FTIR and FT-Raman spectra of the same samples in the $\delta CH_2$ region are depicted in Figs. 5(a) and (b), respectively.

The location and intensity of the $\nu_sCH_2$ mode is complicated due to Fermi resonance between the $\nu_sCH_2$ fundamental with the many overtones of the $\delta CH_2$ vibrations.[32-35] The $\nu_aCH_2$ mode is affected by coupling to the torsional and rotational motions of the chain.[32-35] In the Raman spectrum of alkylene chains in the crystalline state (*all-trans* conformations) the $\nu_aCH_2$ mode is manifested as a strong band in the 2884-2878 $cm^{-1}$ interval, whereas the $\nu_sCH_2$ mode gives rise to bands at 2930 $cm^{-1}$ (weak), 2900-2898 $cm^{-1}$ (medium) and 2850-2844 $cm^{-1}$ (strong).[32-35] In the case of disordered alkylene chains (*gauche* conformations), the $\nu_aCH_2$ was reported at 2897-2890 $cm^{-1}$ and the $\nu_sCH_2$ bands typically appeared at 2920 $cm^{-1}$ (medium), 2904 $cm^{-1}$ (medium) and 2858-2853 $cm^{-1}$ (s).[32,33,35] A shift to higher frequencies and band broadening is therefore correlated with an increase of the proportion of *gauche* conformers.

The Raman $\nu CH_2$ region of the di-amidosil hybrids exhibits two prominent bands centered at 2925 and 2890 $cm^{-1}$ and a shoulder at 2857 $cm^{-1}$ (Fig. 4). The features at 2857 and 2925 $cm^{-1}$,characteristic of disordered alkylene chains, are attributed to the $\nu_sCH_2$ fundamental and to the Fermi resonance between the $\nu_sCH_2$ fundamental with the many overtones of the $\delta CH_2$ vibrations, respectively.[32,33,35] The intense 2890 $cm^{-1}$ event is ascribed to the $\nu_aCH_2$ stretching mode of alkylene chains in the amorphous state.[32,33,35] We may infer from these findings that the alkylene chains of the di-amidosils are fully disordered and adopt, as expected, essentially *gauche* conformations, a conclusion that corroborates the $^{13}C$ CP/MAS NMR, XRD and DSC results.

The frequency, intensity and band shape of the $\delta CH_2$ mode are sensitive to interchain interaction and to packing arrangement of the chains.[36] Higher frequencies (~1472 $cm^{-1}$) in the infrared spectra indicate ordering of the alkylene chains in *all-trans* crystalline state. Lower frequency (~1466 $cm^{-1}$), band broadening and decreasing intensity are indicative of an increase in chain motion (which is normally associated with the liquid state) and consequently in the *gauche*/*trans* conformer ratio.[36] The band centred at about 1466 $cm^{-1}$ in the $\delta CH_2$ regio of the FTIR spectra of the di-amidosil hybrids (Fig. 5(a)) is ascribed to the presence of fully disordered alkylene chains with a high proportion of *gauche* conformers.[36] The 1441 $cm^{-1}$ band detected in the same spectra is indicative of the occurrence of *gauche* bonds.[37] In the FT-Raman spectra of the di-amidosils the $\delta CH_2$ mode appears as a broad event located around 1440 $cm^{-1}$ (Fig. 5(b)). This feature represents an additional proof that the alkylene chains adopt *gauche* conformations.[33]

**Hydrogen bonding** - To evaluate the strength and extension of hydrogen bonding in the d-A(4) and d-A(8) samples we examined the spectral signature of these materials in the amide I (1800-1600 $cm^{-1}$) and amide II (1600-1500 $cm^{-1}$) regions.

The amide I mode (or simply carbonyl stretching mode, $\nu C=O$) is a very complex vibration that receives a major contribution from the C=O stretching vibration and minor contributions from the C-N stretching and C-C-N deformation vibrations.[38]As the C=O stretching vibration is sensitive to the specificity and magnitude of hydrogen bonding, the amide I envelope consists of several distinct components reflecting different environments of the C=O groups, usually designated as aggregates or associations. As the absorption coefficients of C=O groups involved in different aggregates can be different, it is not possible to compare intensity values of different spectral components and thus only the changes undergone by each mode are an adequate reflection of concentration variation of certain type of association.[39,40] Shifts of the $\nu C=O$ mode of the free amide group to lower wavenumbers result upon formation of hydrogen bonded associations.

The amide II mode, mainly associated with the N-H in-plane bending vibration ($\delta_{i.p.}NH$), is sensitive to chain conformation and intermolecular hydrogen bonding, providing information about the distribution of hydrogen bond strengths.[39a] When the

amide group is included in hydrogen bonded aggregates the $\delta_{i.p.}$NH band characteristic of free amide is upshifted.

In the infrared spectra of amorphous polyamides an intense band at 1640 $cm^{-1}$ and a shoulder at about 1670 $cm^{-1}$, attributed to hydrogen-bonded and "free" carbonyl groups, respectively, were found in the amide I region.[39] In the same spectra the amide II band was seen at 1545 $cm^{-1}$.[39]

The room temperature FTIR spectra of the d-A(4) and d-A(8) compounds in the amide I and II regions are reproduced in Fig. 6(a). The results of the curve-fitting performed in 1800-1500 $cm^{-1}$ region are displayed in Fig. 6(b).

The broad amide I envelope of the di-amidosil hybrids exhibits two intensity maxima at 1732 and 1649 $cm^{-1}$ (Fig. 6(a)). The 1732 $cm^{-1}$ band was decomposed into three components at 1755, 1736 and 1713 $cm^{-1}$ (Fig. 6(b)).. The 1649 $cm^{-1}$ band was resolved into three components at 1679, 1652 and 1623 $cm^{-1}$ (Fig. 6(b)). The 1755 $cm^{-1}$ feature is assigned to amide linkages whose N-H and C=O groups are non-bonded. The 1736 and 1713 $cm^{-1}$ components are ascribed to disordered amide-amide aggregates of increasing strength, respectively. The 1679, 1652 and 1623 $cm^{-1}$ features are attributed to the absorption of C=O groups in considerably more ordered hydrogen-bonded amide-amide associations with increased hydrogen bond strength, respectively. The significant number of components required for the deconvolution of the amide I envelope demonstrates the high degree of structural disorder of both samples. It is finally worth emphasizing the high complexity of the amide I envelope of the di-amidosils with respect to the "amide I" band of a di-urethanesil analog.[41] In fact, both types of hybrid systems contain cross-links which are practically the same from the chemical standpoint (one hydrogen donor group and one hydrogen acceptor group). However, while in the di-urethanesil hybrid two different types of hydrogen-bonded associations exist (urethane/POE (1724 cm-1) and urethane-urethane (1696 cm-1)),[41] in the di-amidosils we have identified five different types of environments for C=O groups belonging to amide-amide aggregates (Fig. 6(b)).

The amide II mode of the d-A(4) and d-A(8) samples (Fig. 6(b)), centered at about 1552 $cm^{-1}$, was decomposed into two peaks at 1561 and 1532 $cm^{-1}$, suggesting that hydrogen-bonded aggregates with two hydrogen bond strengths exist in both materials. It is of interest to note that the intensity maximum of the "amide II" band of the di-urethanesil analog is located at 1536 $cm^{-1}$.[41], an indication that the hydrogen bonds in the di-amidosils are significantly stronger than in the di-urethanesils.

**Photoluminescence features**

Fig. 7 shows the PL spectra the d-A(8) and d-A(4) di-amidosils acquired under different excitation wavelengths. All the spectra are composed of a large Gaussian shaped broad band between 380 and 580 nm, the emission energy of which deviates to the red region as the excitation wavelength increases from 300 to 430 nm. For excitation wavelengths lower than 400 nm, the spectrum of the d-A(8) sample is shifted towards the blue (800 $cm^{-1}$) with respect to that of the d-A(4). For excitation wavelengths within 420-440 nm, the energetic difference between the emission of the two di-amidosils decreases to *ca.* 400 $cm^{-1}$. A similar large broad band has already been observed for other classes of analogous organic-inorganic hybrids, classed as di-ureasils, mono- and di-urethanesils.[17-19,31,42] The origin of such band was ascribed to the convolution of donor-acceptor pair (D-A) recombinations that occur in the NH groups of the urea linkages and in the siliceous nanodomains.[17-19] It was recently proposed that the mechanism responsible for the NH-related component is associated with photoinduced proton-transfer between $NH_2^+$ and $N^-$ defects. The chemical nature of the D-A subjacent to the component associated with the siliceous nanodomains was investigated by EPR measurements, that agree with a defect-model similar to that of the well-known peroxy-radical in $SiO_2$, but where the silicon is coordinated to one carbon and two other oxygen atoms: $^{\bullet}O-O-Si\equiv(CO_2)$.[19] Experimental evidence will be presented below in order to illustrate the similarity between the nature of the recombination centres in the di-amidosils and in the di-ureasils, mono- and di-urethanesils. Fig. 8 presents the room temperature PLE spectra of the d-A(8) and d-A(4) di-amidosils monitored along the hybrids emission band showed in Fig 7. The spectra consist of a broad asymmetrical band between 300 and 450 nm. As the monitoring energy decreases, the intensity maximum of the band moves to longer wavelengths and the band becomes broader, an indication of the presence of more than one component. The higher and lower energetic sides can be attributed to the preferential excitation of the emission originated in the siliceous and NH groups, respectively.[18,19] Upon lowering the temperature down to 14 K, apart from an emission blue-shift of *c.a.* 900 $cm^{-1}$ and an increase in the PL intensity, the luminescence features remain essentially the same as those described above for room temperature.

The photoluminescence properties of the di-amidosils, in particular those of the d-A(8), were further investigated through time-resolved spectroscopy. These measurements were performed at low-temperature because the time-scale of the luminescence properties is smaller that the detection limit of our experimental setup ($10^{-5}$ s). Fig. 9 shows the time resolved PL obtained at different starting delays. For the shorter starting delays (0.05-5.00 ms) the spectra reveal the presence of three main peaks centred at *ca.* 425, 460 and 500 nm, whereas for starting delays higher than 5.00 ms, only the lower energetic peak can be discerned. This indicates that the components at 425 and 460 nm may have the same nature, whereas the band at *c.a.* 500 nm must have a different origin. From the comparison of these results with those previously obtained for the similar organic-inorganic hybrids,[17] we may ascribe the two higher energetic peaks and the lower energy band as siliceous- and NH-associated components, respectively. Lifetime measurements were performed by monitoring the three peaks in the time-resolved spectra of Fig. 9. For starting delays of 0.05 ms, the decay curves revealed a non-exponential behaviour, characterized by a mean decay time value ($\tau_{10}$) for which the maximum PL intensity is reduced to 1/10 of its maximum intensity. For the longer-lived NH-related emission and for the siliceous-based one, $\tau_{10}$ values of *ca.* 160±20, and 2.0±0.1 ms, respectively, were found. Such lifetime values are similar to those previously reported for the di-ureasils,[17] indicating that the recombination time scale is similar in both nanocomposites. Another similarity between the two families of hybrids lies on the physical origin of the PL related components.

The distinction between the various near band-edge transitions (free exciton, bound exciton, free carrier to neutral acceptor-donor (D-A), and D-A pairs) that occur in crystalline semiconductors can be made through the analysis of the emission intensity dependence on the excitation power.[19,43] The emission intensity ($I$) depends on the excitation power ($L_{exc}$) according to the power law:

$$I \alpha L_{exc}^{k} \quad (3)$$

when $1 < k < 2$ we are in the presence of exciton-like transitions; $k \leq 1$ is characteristic of free-to-bound and D-A pairs.[19,43] Fig.10 (a) depicts the integrated intensity for the d-A(8) steady-state emission calculated for different magnitudes of the excitation power. The integrated intensity of both components was obtained independently using the curve-fitting procedure described elsewhere.[31,42] The integrated intensity of both PL components depends sub-linearly on the power excitation, with a $k$ value of 0.98 ± 0.09 and 1.05 ± 0.02 for the NH- and siliceous-related emissions. This is a clear indication that both emissions revealed a recombination mechanism typical of D-A pairs, mediated by some localized centres. [19,43]

Further experimental evidence enabling the identification of D-A transitions can be obtained from time-resolved emission acquired at different starting delays. For longer delay times, a red shift in the spectrum is expected because distant pairs have a smaller recombination probability. The respective energy levels therefore have larger lifetimes, a situation that is favoured with the increasing delay time. As a consequence, the recombination takes place at lower energies. The spectra of Fig 9 were fitted assuming the overlap of three distinct components for starting delays ≤ 5.00 ms; for higher starting delays the spectra were well reproduced by a single Gaussian function. Fig. 10(b) shows, for the d-A(8) di-amidosil, the energetic shift between the energy of the maximum intensity of the time-resolved spectra (derived the fit to the spectra in Fig. 9) and the corresponding value detected under continuous excitation. Changing the starting delays from 0.05 ms to 5.00 ms, the blue-band emission shifts toward the red region and for starting delays within 5.00-50.00 ms, the recombination always occurs at *ca.* 2.47 eV. The decrease of the emission energy with the starting delay is consistent with D-A pair recombination.[19,43c]

With respect to the purplish-blue band, the results are restricted to the starting delay interval between 0.05 and 3 ms because this emission occurs on a time scale two orders of magnitude lower than the blue-band recombination processes. For such starting delay interval, an emission red-shift of *ca.* 0.07 eV between the steady-state and time-resolved emission spectra was observed. In agreement with what has been recently demonstrated for other organic-inorganic hybrids,[19] the d-A(8) di-amidosil emission components display a typical D-A pair recombination mechanism.

**Absolute emission quantum yields**

The absolute emission quantum yields were measured for the d-A(8) for excitation wavelengths within 350-440 nm, as listed in Table III. The maximum quantum yield value (5.4 %) was obtained under the excitation wavelength of 375 nm as this wavelength corresponds to the maximum peak position in the PLE spectra (Fig. 8). At this excitation wavelength, both emission components (NH and siliceous nanodomains) contribute to the overall emission.

Comparing these values with those reported for other organic-inorganic hybrids prepared via conventional hydrolysis, such as the di-ureasils and di-urethanesils,[17] we find out that the d-A(8) maximum quantum yield value is similar to that of a di-ureasil hybridwhich incorporates oligopolyether chains with about 8.5 oxyethylene repeat units, but is smaller than the values reported di-ureasils and di-urethanesils hybrids with longer polymer chains.[17,18] The maximum quantum yield value of the d-A(8) di-amidosil is also smaller than those of di-ureasils synthesized through carboxylic acid solvolysis.[18] The differences in the quantum yield values of such organic-inorganic hybrids was recently related with the degree of the hydrogen bonds established between adjacent urea/urethane groups.[18,19] The presence of stronger hydrogen bonds contributes to localize the proton, thus rendering difficult the induced transfer of the hydrogen atoms between NH groups.[18,19] Consequently, the NH_related emission quantum yield will be smaller. This PL component is selective excited for excitation wavelengths higher than 420 nm,[19,43] revealing for the d-A(8) di-amidosil a quantum yield around 3.8 %. For the luminescence originated in the siliceous nanodomains it is not possible to quantify the respective $\phi$ value independently, because at the excitation wavelength range used there is no selective excitation for that emission. The quantum yield value of the NH-related emission measured for the selective excitation wavelength of 440 nm is smaller than the values found for the di-ureasil and di-urethanesil hybrids,[19] suggesting that proton transference processes in the d-A(8) structure are not favoured. We feel tempted to suggest that this fact results very likely from the high degree of disorder of the very strong hydrogen-bonded amide-amide associations formed throughout the material. We may further venture that the alkylene chains must play a key role in the establishment of this disordered array of amide-amide aggregates.

**Conclusions**

In the present work we investigated innovative amide cross-linked alkylene/siloxane hybrids designated as di-*amidosils*. Two samples with short chains d-A(4) and d-A(8) (where 4 and 8 represent the number of methylene groups per chain) were analyzed. These xerogels, obtained as transparent, amorphous rigid monoliths with a yellowish hue, are thermally stable up to about 380-400 ºC. The estimated interdomain distances are 12 and 17 Å, respectively. The siliceous network of d-A(8) is composed of $T^3$ [$(SiO)_3Si(CH_2)$-] and $T^2$ [$(SiO)_2(HO)Si(CH_2)$-] environments. The analysis of the FTIR, FT-Raman and $^{13}C$ CP/MAS RMN spectra revealed that the alkyl chains in both di-amidosils are in a disorder state and adopt essentially *gauche* conformations. FTIR provided evidence that in these samples the amide groups are extensively involved in the formation of a disordered array of strong amide-amide hydrogen bonded associations with different hydrogen bond strengths. The hybrids investigated are room temperature white light emitters, presenting an emission large, broad band in the blue/purplish-blue spectral region. The origin of such band was ascribed to the convolution of donor-acceptor pair (D-A) recombinations that occur in the NH groups of the urea linkages and in the siliceous nanodomains. The maximum quantum yield value of the d-A(8) di-amidosil is

5.4 %, similar to those of analogous organic/inorganic hybrids (di-ureasils ands di-urethanesils). The selective excitation of the NH-related emission permits the determination of an emission quantum yield of 3.8 %. This value is smaller than the values found for the di-ureasil and di-urethanesil hybrids, suggesting that proton transference processes in the d-A(8) structure are not favoured, probably due to the high degree of disorder of the very strong hydrogen-bonded amide-amide associations formed throughout the material.

**Acknowledgement**

This work was supported by Fundação para a Ciência e Tecnologia (POCTI/P/CTM/46780/03 and SFRH/BD/13559/03). S. C. Nunes acknowledges Fundação para a Ciência e Tecnologia for a grant.

**S. C. Nunes[a], V. de Zea Bermudez[a], R. A. Sá Ferreira[b], L. D. Carlos[b], M. M. Silva[c], M. J. Smith[c], D. Ostrovskii[c], J. Rocha[e]**

[a]Departamento de Química and CQ-VR, Universidade de Trás-os-Montes e Alto Douro, 5000-911 Vila Real, Portugal. Fax: +351-259-350480; Tel: +351-259-350253;

[b]Departamento de Física and CICECO, Universidade de Aveiro, 3810-193 Aveiro, Portugal *Fax: +351-234-424965; Tel: +351-234-370946; E-mail: lcarlos@fis.ua.pt*

[c]Departamento de Química, Universidade do Minho, Gualtar, 4710-057 Braga, Portugal *Fax: +351-253-678983; Tel: +351-253-676376; E-mail: mjsmith@quimica.uminho.pt*

[d]Department of Applied Physics, Chalmers University of Technology, 41296 Göteborg, Sweden *Fax: +46-31-772-317; Tel: +46-31772-8038; E-mail: dostr@fys.chalmers.se*

[e]Departamento de Química and CICECO, Universidade de Aveiro, 3810-193 Aveiro, Portugal, *Fax: +351-234-370084 Tel: +351-234-370730; E-mail: rocha@quimica.ua.pt*

## Notes and references

† Peakfit is a product of Jandel Corporation, 2591 Rerner Boulevard, San Rafael, CA 94901, U.S.A.

1 Functional Hybrid Materials, Gomez-Romero, P. and Sanchez, C. Editors, Wiley Interscience, New York, 2003.

2 R. Laine, C. Sanchez, C. J. Brinker, E. Gianellis (Eds), *Organic/Inorganic Hybrids Materials*, Materials Research Society Series, Vol. 628, Pittsburgh, PA, 2000.

3 B. Lebeau, C. Sanchez, *Curr. Opin. Solid State Mater. Sci*., 1999, **4,** 11.

4 C. Sanchez, B. Lebeau, *Mater. Res. Soc. Bull*., ed. *D. A. Loy,* Vol. 26, 2001, 377.

5 C. J. Brinker, G. Scherer, *Sol-gel Science: The Physics and Chemistry of Sol-Gel Processing*, Academic Press, San Diego, CA, 1990.

6 C. Sanchez, F. Ribot, B. Lebeau, *J. Mater. Chem.*, 1999, **9**, 35.

7 H. Li, S. Inoue, D. Ueda, K. Machida, G. Adachi, *Electrochem. Solid State Letter*, 1999, **2**, 354.

8 M. Faloss, M. Canva, P. Georges, A. Brun, F. Chaput, J.-P. Boilot, *Appl. Opt,* 1997, **36**, 6760.

9 D. Blanc, S. Pellisier, K. Saravanamuttu, S. I. Najafi, M. P. Andrews, *Adv. Mater.*, 1999, **11**, 1508.

10 R. Buestrich, F. Kahlenberg, M. Popall, P. Dannberg,, R. M.-Fiedler, O. Rösch, *J. Sol-Gel Sci. Technol.*, 2001, **20**, 181.

11 T. Dantas de Morais, F. Chaput, J.-P. Boilot, K. Lahlil, B. Darracq, Y. Levey, *Adv. Mater.* 1999, **11**, 107.

12 D. B. Mitzi, K. Chondroudis, C. R. Kagan, *IBM J. Res. & Dev*., 2001, **45**, 29.

13 W. H. Green, K. P. Le, J. Grey, T. T. Au, M. J. Sailor, *Science*, 1997, **276**, 1826.

14 V. Bekiari, P. Lianos, *Chem. Mater.***,** 1998, **10**, 3777.

15 Y. Uchida, Y.-I. Nobu, I. Momiji, K. Matsui, *J. Sol-Gel Sci. Tech*., 2000, **19**, 705.

16 Y. Han, J. Lin, *J. Solid State Chem.,* 2003, **171**, 396.

17 L. D. Carlos, R. A. Sá Ferreira, V. de Zea Bermudez, S. J. L. Ribeiro, *Adv. Funct. Mater*., 2001, **11(2)**, 111

18 L. Fu, R. A. Sá Ferreira, N. J. O. Silva, L. D. Carlos, V. de Zea Bermudez, J. Rocha, *Chem. Mater.*, 2004, **16**, 1507.

19 L. D. Carlos, R. A. Sá Ferreira, R. N. Pereira, M. Assunção, V. de Zea Bermudez, *J. Phys. Chem. B*., 2004, **108**, 14924.

20 S. C. Nunes, V. de Zea Bermudez, D. Ostrovskii, M. M. Silva, S. Barros, J. M. Smith, L. Carlos, J. Rocha, E. Morales, *J. Elect. Soc.,* 2005, **152(2)**, A429.

21 A.-C. Franville, R. Mahiou, D. Zambon, J.-C. Cousseins, *Solid State Sciences*, 2001, **3**, 211.

22 J. J. E. Moreau, L. Vellutini, M. Wong Chi Man, C. Bied, J.-L. Bantignies, P. Dieudonné, J.-L. Sauvajol, *Mat. Res. Soc. Symp. Proc.* Vol. 726, **Q 7.2.1**.

23. J. J. E. Moreau, L. Vellutini, M. Wong Chi Man, C. Bied, P. Dieudonné, J.-L. Bantignies, J.-L. Sauvajol, *Chem. Eur. J.,* 2005, **11**, 1527.

24. S.-I. Han, B.-S. Kim, S.-W. Kang, H. Shirai, S. S. Im, *Biomaterials*, 2003, **24**, 3453

25. Y. Fan, M. Kobayashi,H. Kise, *J. Polym. Sci. A: Polym. Chem.*, 2001, **39**, 1318

26 A. Brill and A. W. De Jager-Veenis, *J. Electrochem. Soc.*, 1976, **123**, 396.

27 (a) A. Shimojima, Y. Suguhara, K. Kuroda, 1997, **70**, 2847; (b) M. Pursch, A Jäger, T. Schneller, R. Brindle, K. Albert, E. Lindner, *Chem. Mater.*, 1996, **8**, 1245; (c) A. N. Parikh, M. A. Schivley, E. Koo, K. Seshadri, D. Aurentz, K. Mueller, D. L. Allara, *J. Am. Chem. Soc*., 1997, **119**, 3135

28 L. D. Carlos, R. A. Sá Ferreira, I. Orion, V. de Zea Bermudez, J. Rocha, *J. Luminesc*., 2000, **87-89**, 702.

29 M. C. Gonçalves, V. de Zea Bermudez, R. A. Sá Ferreira, L. D. Carlos, D. Ostrovskii, J. Rocha, *Chem. Mater*., 2004, **16(13)**, 2530.

30 L. D. Carlos, V. de Zea Bermudez, R. A. Sá Ferreira, L. Marques, M. Assunção, *Chem. Mater*., 1999, **11(3)**, 581

31 K. Dahmouche, C. V. Santilli, S. H Pulcinelli, A. F. Craievich, *J. Phys. Chem. B*, 1999, **103**, 4937

32 R. G. Snyder, H. L. Strauss, C. A. Ellinger, *J. Phys. Chem*. 1982, **86,** 5145.

33 R. Wang, G. Baran, S. L. Wunder, *Langmuir*, 2000, **16(15),** 6301

34 (a) N. V. Venkataraman, S. Vasudevan, *J. Phys Chem B,* 2001, **105(32)**, 7639; (b) N. V. Venkataraman, S. Bhagyalakshmi, S. Vasudevan, R. Seshadri, *Phys. Chem. Chem. Phys.* 2002, **4**, 4533

35 K. G. Brown, E. Bicknell-Brown, M. Ladjadj, *J. Phys. Chem.* 1987, **91**, 3436

36 R. A. Vaia, R. K. Teukolsky, E. P. Gianneli, *Chem. Mater*., 1994, **6,** 1017.

37 (a) H. Hagemann, H. L. Strauss, R. G. Snyder, Macromolecules, 1987, **20**, 2810; (b) G. Zerbi, M. Del Topp, in Modern Polymer Spectroscopy, G. Zerbi (Editor), Wiley-VCH, Weinheim, 1999

38 Miyazawa, T. Shimanouchi, S.-I. Mizushima, *J. Chem. Phys.,* 1956, **24 (2)**, 408

39 (a) *D.* J. Skrovanek, S. E. Howe, P. C. Painter, M. M. Coleman, *Macromolecules,* 1985, **18**, 1676; (b) D. J. S Skrovanek, P. C. Painter, M. M. Coleman, *Macromolecules*, 1986, **19**, 699

40 D. J. S Skrovanek, P. C. Painter, M. M. Coleman, *Macromolecules*, 1986, **19**, 2149

41 M. C. Gonçalves, N. J. O. Silva, V. de Zea Bermudez, K. Dahmouche, C. V. Santilli, A. F. Craievich, R. A. Sá Ferreira, L. D. Carlos, D. Ostrovskii, I. C. Correia Vilela, submitted

42 R. A.Sá Ferreira, L. D. Carlos, V. de Zea Bermudez, *Thin Solid Films*, 1999, **343**, 470.

43 (a) R. A. Street, *Adv. Phys.* 1981, **30**, 593. (b) T. Schmidt, K. Lischka, W. Zulehner, *Phys. Rev. B*, 1992, **45**, 8989. (c) J. I. Pankove, *Optical Processes in Semiconductors*; Dover Publications: New York, 1990; (d) K. S. Zhuravlev, A. M. Gilinsky, A. Y. Kobitsky, *Appl. Phys. Lett.* 1998, **73**, 2962.

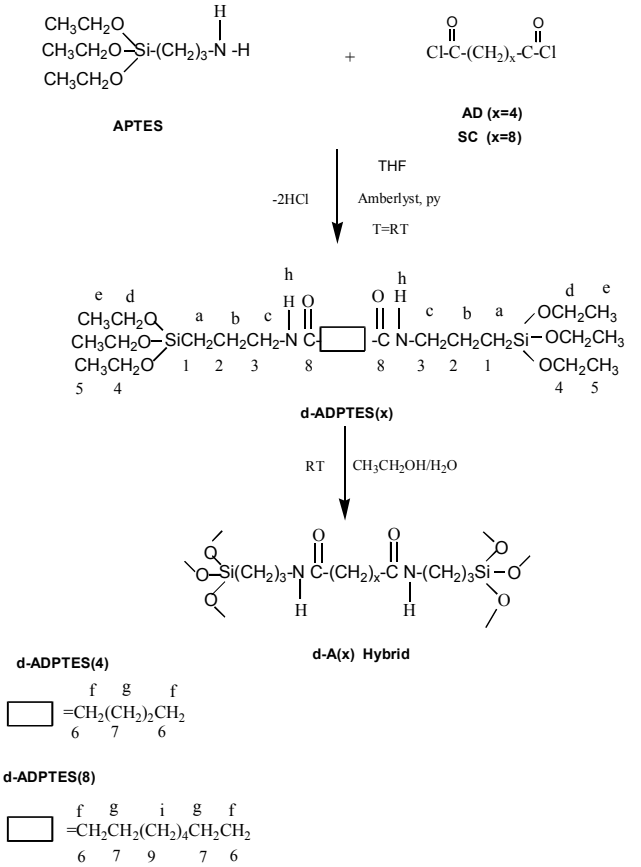


**Scheme 1 -** Synthetic procedure of the d-A(x) di-amidosils.

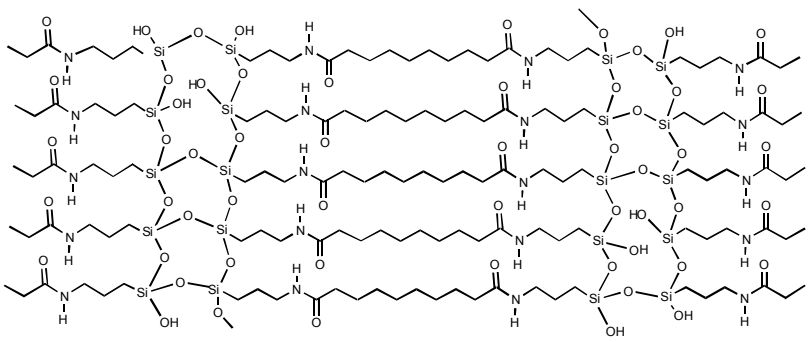

**Scheme 2 -** Structure of d-A(8) di-amidosil

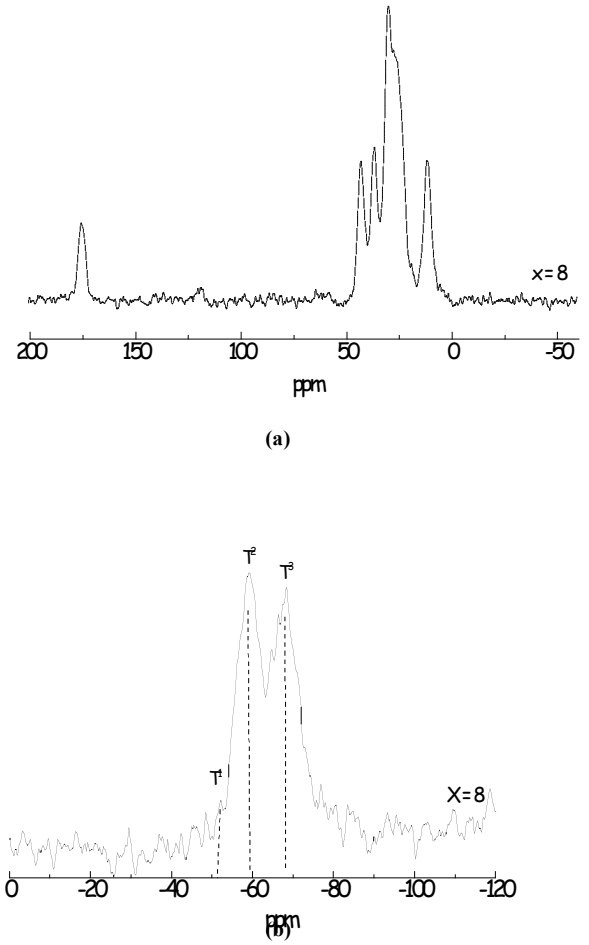


**Fig. 1** - $^{13}C$ CP/MAS (a) and $^{29}Si$ MAS (b) NMR spectra of the d-A(x) di-amidosils.

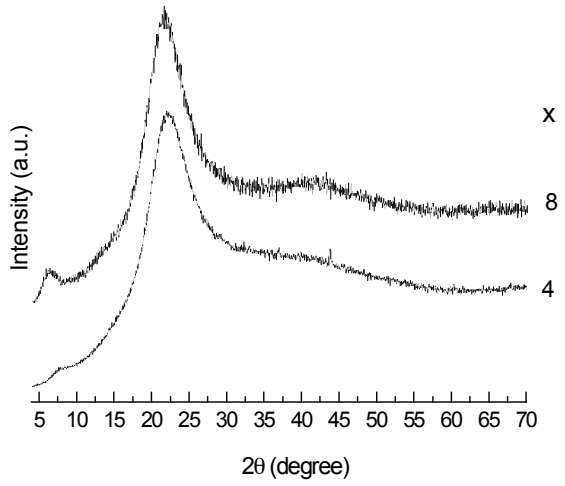


**Fig. 2** - XRD patterns of the d-A(x) di-amidosils.

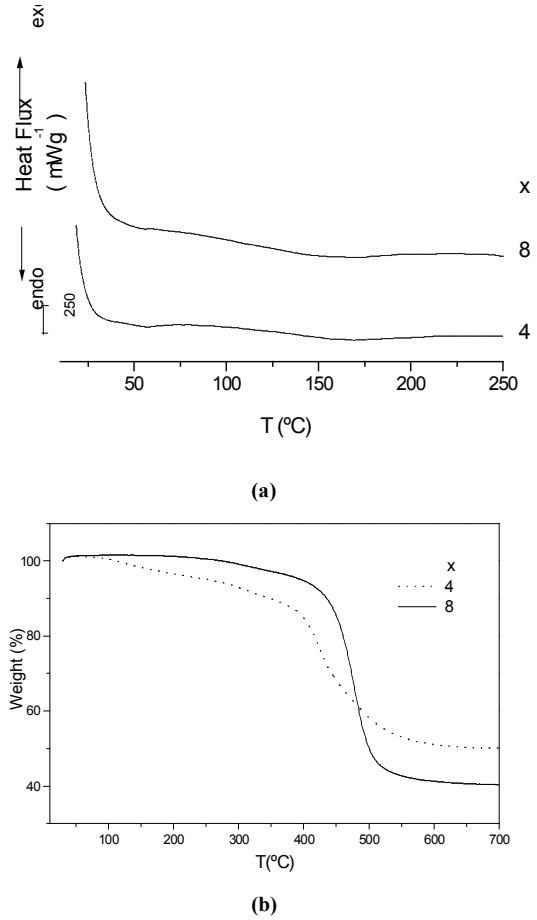


**Fig. 3** - DSC (a) and TGA (b) curves of the d-A(x) di-amidosils.

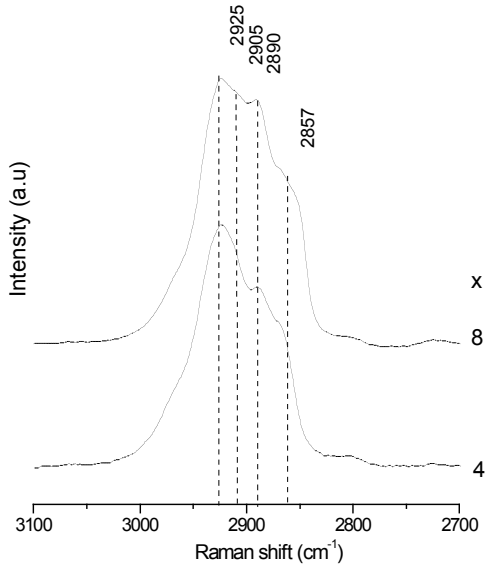


**Fig. 4** – Room temperature FT-Raman spectra of the d-A(x) di-amidosils in the $\nu_s CH_2$ and $\nu_a CH_2$ regions.

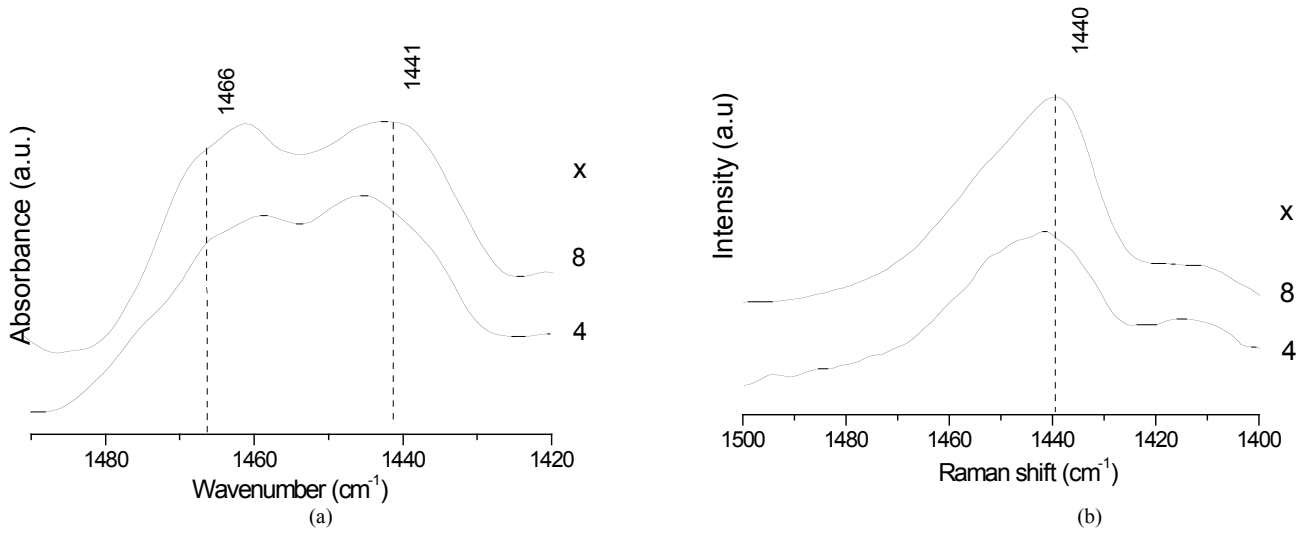


**Fig. 5** Room temperature FTIR spectra (a) and room temperature FT-Raman (b) of the d-A(x) di-amidosils in the $\delta CH_2$ region.

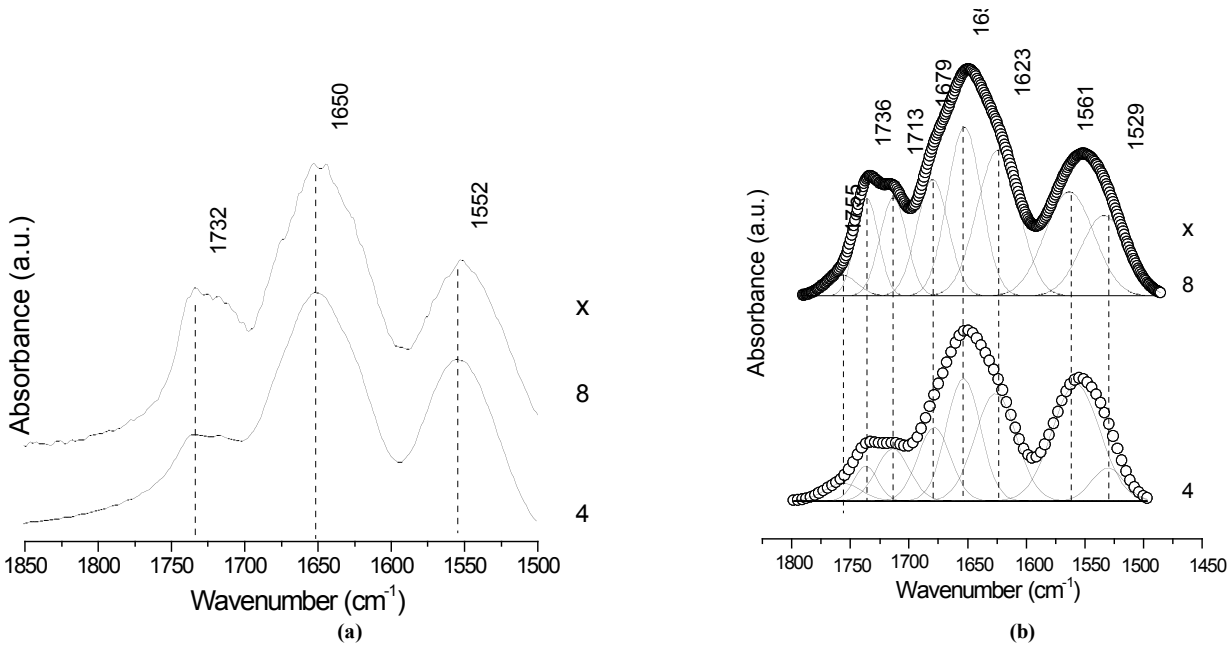


**Fig. 6 -** Room temperature FTIR spectra (a) and curve-fitting results (b) of the d-A(x) di-amidosils in the amide I and amide II regions.

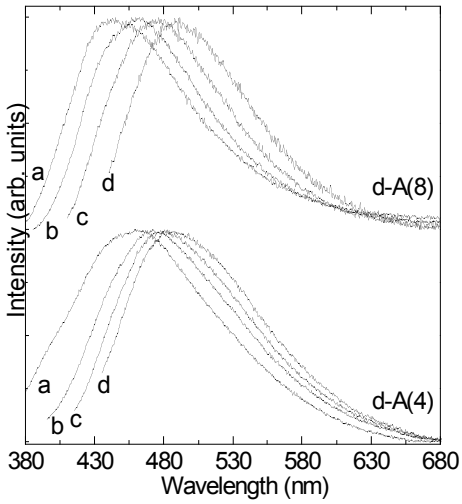


**Fig. 7 –** PL spectra (300K) of the d-A(4) and d-A(8) di-amidosils at different excitation wavelengths (a) 350, (b) 375, (c) 400, and (d) 430 nm.

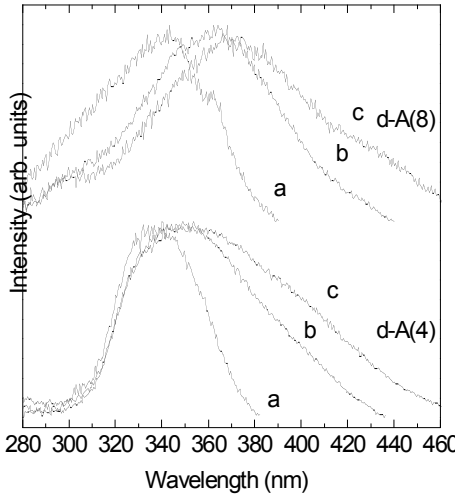


**Fig. 8 –** PLE spectra (300K) of the d-A(4) and d-A(8) di-amidosils at different monitoring wavelengths (a) 395, (b) 446, and (c) 480 nm.

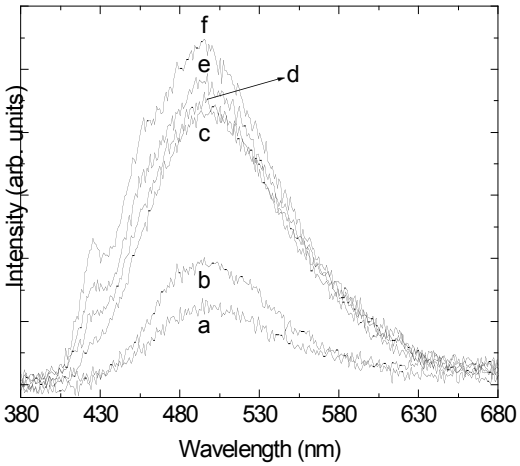


**Fig. 9 –** Time-resolved PL spectra (14 K) of the d-A(8) di-amidosil at an excitation wavelength of 360 nm for different starting delays (a) 0.05, (b) 1.00, (c) 3.00, (d) 5.00, (e) 20.00 and (d) 50.00 ms.

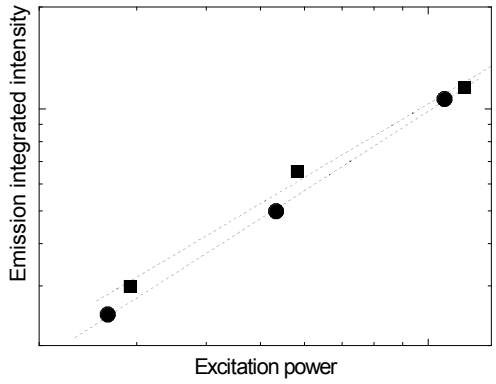


(a)

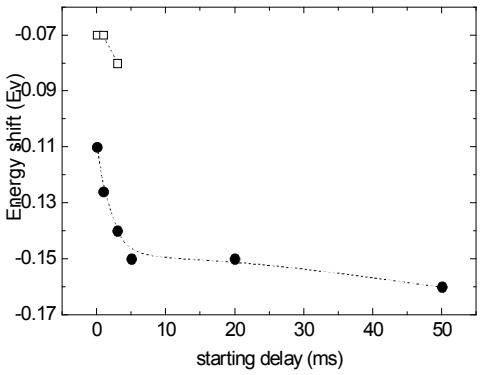


(b)

**Fig. 10 –** (a) Integrated intensity for the d-A(8) di-amidosil NH-related emission and siliceous-based component measured at different power excitations. The dashed lines correspond to linear fits to the data (R = 0.99). (b) Energetic shift of the NH- and siliceous related emissions between the energy of the maximum intensity of the time-resolved spectra and the corresponding value measured under continuous excitation. The dashed lines are guides to the eyes. The solid circle and the open square are ascribed to the NH- and siliceous associated emissions, respectively.

**Table I -** $^{1}$H and $^{13}$C NMR data of the d-ADPTES(x) di-amidosil precursors.

| $^{1}$H | | | | | | | | $^{13}$C | | | | |
|---|---|---|---|---|---|---|---|---|---|---|---|---|
| x = 4 | Attribution | | x = 8 | Attribution | | Ref. | x = 4 | Attribution | x = 8 | Attribution | Ref. |
| 4.07-4.13 | q | 2H H$^{h}$ | 4.09-4.03 | q | 2H H$^{h}$ | | 176.32/173.34 | C$^{8}$ | 173.77 | C$^{8}$ | |
| 3.73-3.61 | m | 12H H$^{d}$ | 3.79-3.60 | m | 12H H$^{d}$ | 20-22 | 58.33 | C$^{4}$ | 58.07 | C$^{4}$ | 21,22 |
| | | | 3.18-2.97 | m | 4H H$^{c}$ | 20-22 | - | C$^{3}$ | 41.70 | C$^{3}$ | 20-22,25 |
| 2.34-2.24 | q | 8H H$^{f}$, H$^{c}$ | 2.27-2.09 | q | 4H H$^{f}$ | 21-24 | 33.93-33.41 | C$^{6}$ | 34.24 | C$^{6}$ | 23-25 |
| 1.65-1.62 | q | 8H H$^{g}$ ,H$^{b}$ | 1.56-1.45 | s,b | 8H H$^{g}$,H$^{b}$ | 20-24 | | | 29.10-28.94 | C$^{9}$ | 22-25 |
| 1.24-1.19 | q | 18H H$^{e}$ | 1.25-1.15 | m | 26H H$^{e}$, H$^{i}$ | 20-23 | 24.37-24.34 | C$^{2}$ | 24.82 | C$^{2}$ | 20-22,25 |
| 0.6 | t | 4H H$^{a}$ | 0.60-0.57 | t | 4H H$^{a}$ | 20-22 | 24.21 | C$^{7}$ | 22.80 | C$^{7}$ | 23-25 |
| | | | | | | | 18.34 | C$^{5}$ | 18.26/18.17 | C$^{5}$ | 20-22,25 |
| | | | | | | | 14.18 | C$^{1}$ | 7.31 | C$^{1}$ | 20-22,25 |

[a] m – multiplet, q - quartet, t – triplet, s – singlet and b – broad

**Table II** - $^{29}$Si MAS and $^{13}$C CP/MAS NMR data of the d-A(8) di-amidosil.

| $^{29}$Si | | | $^{13}$C | |
|---|---|---|---|---|
| δ (ppm) | (%) | Attribution | δ (ppm) | Attribution |
| -51.6 | ( 0.9) | T$^{1}$(R-Si(OSi)(OH)$_2$) | 174 | C$^{8}$ |
| -58.8 | (52.6) | T$^{2}$ (R-Si(OSi)$_2$(OH)) | 42 | C$^{3}$ |
| -67.8 | (46.5) | T$^{3}$ (R-Si(OSi)$_3$) | 35 | C$^{6}$ |
| | | | 29 | C$^{9}$ |
| | | | 26 | C$^{2}$ |
| | | | 25 | C$^{7}$ |
| | | | 11 | C$^{1}$ |

[a] Footnote text.

**Table III** – Room temperature absolute emission quantum yields (ϕ) for the d-A(8) di-amidosil for different excitation wavelengths ($\lambda_x$).

| $\lambda_{x\,(nm)}$ | 350 | 365 | 375 | 400 | 440 |
|---|---|---|---|---|---|
| **ϕ (%)** | 3.1 | 4.2 | 5.4 | 3.4 | 3.8 |